https://doi.org/10.1007/s41230-026-5206-2

Effect of critical tempering on microstructure evolution, mechanical performance, and corrosion behavior of a cast multiphase stainless steel

Jing-yu He[1], **Guo-qiang Liu[2], Zi-xiang Wu[3], Hua-wei Zhang[1, 4], and *Xiang Chen[1, 4]

1. School of Materials Science and Engineering, Tsinghua University, Beijing 100084, China

2. Inner Mongolia First Machinery Group Co., Ltd., Baotou 01402, Inner Mongolia, China

3. Nano and Heterogeneous Materials Center, School of Materials Science and Engineering, Nanjing University of Science and Technology, Nanjing 210094, China

4. Key Laboratory for Advanced Materials Processing Technology, Ministry of Education, Beijing 100084, China

Abstract: A novel cast stainless steel featuring a multiphase microstructure and a nominal composition of Fe-13.5Cr-2.6Si-6.9Ni-1.1Cu-1.1Mn-1.0Mo-0.35Al-0.025C (wt.%) was investigated. Following solution treatment at 1,050 °C and water quenching, the specimens were subjected to further tempering at 570 °C, 610 °C, and 650 °C to explore the effects of critical tempering on microstructure, mechanical properties, and corrosion resistance. Various characterization techniques were employed to examine the phase distribution within the microstructure, with particular attention given to the content and morphology of reverted austenite. Tensile and corrosion tests were carried out to evaluate the performance of the specimens. The results reveal that critical tempering significantly enhances the mechanical properties, with the specimen tempered at 610 °C achieving the highest product of strength and elongation (PSE=23.6 GPa·%), whereas corrosion resistance deteriorates with increasing tempering temperature. Calculations of the martensite start temperature (M_s) and stacking fault energy (γ_{SFE}) for the reversed austenite in different specimens indicate that the stability of reversed austenite strongly influences mechanical behavior through the TRIP and TWIP effects. However, tempering-induced Cr segregation at ferrite/martensite interfaces and the formation of Cr-depleted zones become more pronounced at higher tempering temperatures, leading to a degradation in corrosion resistance. Furthermore, multiphase coordinated deformation improves the strength-ductility balance, while corrosion tends to initiate at chemically inhomogeneous phase boundaries.

Keywords: cast stainless steel; multiphase structure; stability of reverted austenite; TRIP and TWIP; corrosion resistance

CLC numbers: TG142 **Document code:** A **Article ID:** 1672-6421(2026)03-421-14

1 Introduction

With the growing demand for enhanced mechanical performance in steels and the challenge of overcoming the traditional strength-ductility trade-off, the construction of multiphase, multiscale, and metastable (M^3) microstructures have become an increasingly popular strategy among researchers in recent years[1]. Compared with single-phase ferritic or austenitic stainless steels, duplex stainless steels exhibit superior strength and corrosion resistance. Additionally, martensitic precipitation-hardened stainless steels offer better comprehensive properties than conventional martensitic steels. Therefore, the development of multiphase stainless steels presents a promising research direction.

Several studies have demonstrated the potential of multiphase stainless steels. Tavares et al.[2, 3] reported a martensite-based triphase stainless steel containing

***Xiang Chen**

Male, born in 1970, Ph. D., Professor. His research interests mainly focus on casting alloys, porous metals, and composites. He has published over 200 papers in international and domestic journals. He is the secretary of the WFO Ferrous Metals Commission.

E-mail: xchen@tsinghua.edu.cn

****Guo-qiang Liu**

E-mail: nmyjlgq1101@163.com

Received: 2025-08-23; Revised: 2025-09-25; Accepted: 2026-03-23

37% ferrite and 7.4% reverted austenite, achieving an ultimate tensile strength exceeding 800 MPa along with elongation over 20%. Liu et al.[4, 5] further increased the Ni content to approximately 5.5wt.% to enhance the austenite fraction, achieving elongations beyond 36%, and conducted detailed investigations into the corrosion and hydrogen embrittlement behaviors.

Building upon these advances, Wu et al.[6-8] developed a novel triphase stainless steel based on the PH13-8 martensitic precipitation-hardened system by introducing ferrite through high Si addition and forming reverted austenite via critical tempering after quenching. The resulting steel exhibited an ultimate tensile strength greater than 1,000 MPa and an elongation exceeding 15%. Silicon not only provides substantial solid solution strengthening but also synergizes with chromium to promote the formation of a stable oxide passive film on the steel surface, thus positively influencing both mechanical properties and corrosion resistance[9-11].

The stabilization of reverted austenite generated during tempering plays a pivotal role in enhancing the comprehensive performance of multiphase stainless steels. Reverted austenite improves mechanical properties through transformation-induced plasticity (TRIP) and twinning-induced plasticity (TWIP) mechanisms[12-14]. The stability of retained austenite has been extensively studied in martensitic stainless steels. Xiong et al.[15] achieved improved strength and elongation in 15Cr supermartensitic stainless steel through annealing below the transformation temperature to stabilize austenite. Similarly, He et al.[16] enhanced the elongation of 13Cr supermartensitic stainless steel to over 20% by incorporating nitrogen and employing an innovative heat treatment known as QAP, which combines intercritical annealing (A) with quenching and partitioning (QP). In addition, Zhao and Wang et al.[17, 18] independently demonstrated that the presence of reverted austenite after tempering significantly increases the passive film thickness, thereby improving the corrosion resistance of 13Cr supermartensitic stainless steels.

So far, the tempering process of conventional martensitic stainless steels has been extensively studied, and relatively mature conclusions have been established. However, for newly developed multiphase stainless steels, research remains limited due to their recent emergence. Existing studies have mainly focused on the final microstructure and properties, or have only provided brief descriptions of the deformation process, while systematic investigations into the influence of processing parameters are still scarce. In particular, critical tempering, as the key step for achieving superior comprehensive performance in multiphase stainless steels, has not yet been thoroughly and systematically studied. Thus, it is necessary to systematically investigate the effects of tempering on the microstructure and properties of multiphase stainless steels to optimize heat treatment strategies and fully realize their performance potential. In this study, a newly designed Fe-13.5Cr-2.6Si-6.9Ni-1.1Cu-1.1Mn-1.0Mo-0.35Al-0.025C (wt.%) cast multiphase stainless steel was employed to systematically explore the effects of critical tempering (570 °C, 610 °C, and 650 °C) on microstructural evolution, reverted austenite stability, mechanical properties, and corrosion behavior. The deformation mechanisms and corrosion processes were further elucidated from a composition-microstructure-property perspective.

2 Experiments and methods

In this study, a cast stainless steel was specifically designed with a multiphase microstructure by balancing strength, toughness, and corrosion resistance. Its nominal composition is Fe-13.5Cr-2.6Si-6.9Ni-1.1Cu-1.1Mn-1.0Mo-0.35Al-0.025C (wt.%), as detailed in Table 1. The alloying elements were selected to optimize austenite phase stability (Ni, Mn), promote precipitation hardening of the matrix during heat treatment (Ni, Al, Cu) and improve corrosion resistance (Cr, Mo). A relatively high Si content was deliberately adopted, as it provides significant solid-solution strengthening and, in synergy with Cr, promotes the formation of a protective passive film, thereby contributing positively to both mechanical performance and corrosion resistance. Ingots (~5 kg) were produced by vacuum induction melting, homogenized at 1,050 °C for 1 h, and water-quenched to reduce segregation. Due to the ferrite-stabilizing effect of Si, δ-ferrite remained in the solution-treated sample (designated S1050). Subsequent tempering at 570 °C, 610 °C, and 650 °C yielded ST570, ST610, and ST650, respectively (Fig. 1).

After solution treatment at 1,050 °C and water quenching, austenite transformed into martensite. The δ-ferrite in stainless steels is difficult to eliminate through heat treatments below 950 °C[19], resulting in its presence in the microstructure. Subsequent tempering induced reverted austenite, leading to a triphase microstructure consisting of ferrite, martensite, and

Table 1: Chemical compositions of the experimental steel (wt.%)

C	Si	Mn	Cr	Ni	Mo	Cu	Al	Fe
0.024	2.58	1.08	13.48	6.89	0.97	1.11	0.35	Bal.

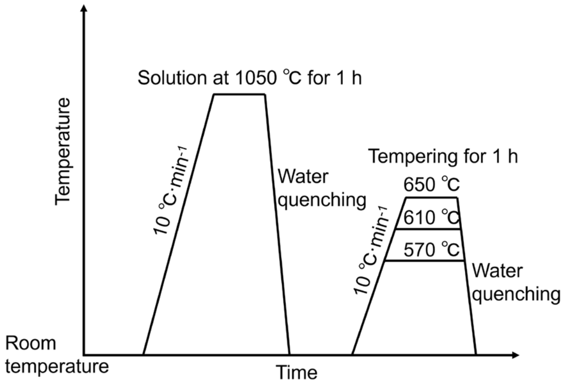

Fig. 1: Heat treatment procedure schematic for the experimental steel

austenite in the ST specimens. The specimens were ground, mechanically polished, and subsequently etched according to the method proposed by Lichtenegger and Bloech[20] to visualize δ-ferrite by optical microscopy (OM). The austenite fraction was determined by X-ray diffraction (XRD), and the remaining phase was considered to be martensite, allowing the phase fractions of the triphase microstructure to be quantified.

Microstructural characterization was conducted using OM, scanning electron microscopy (SEM), electron backscatter diffraction (EBSD), transmission electron microscopy (TEM), and XRD. Optical micrographs were captured using a ZEISS Gemini 2 microscope. SEM and EBSD were performed using a TESCAN S9000X system. Specimens for SEM observation were polished and then etched in a 15% HCl-$FeCl_3$ solution, while EBSD specimens were prepared by electrochemical polishing (10% $HClO_4$+90% CH_3COOH, 20–25 V, 0.05 mA). EBSD data were analyzed with AZtecCrystal to obtain phase distribution maps, band contrast (BC) maps, Kernel average misorientation (KAM) maps, and grain boundary (GB) maps. TEM foils were thinned to ~50 μm, punched into 3 mm disks, and ion-milled using 4 kV Ar^+ ions at 7°–8°, with observations conducted on a JEM-2100 microscope. The XRD patterns were refined using the Rietveld method implemented in Maud software to determine the volume fraction of austenite. Additionally, Thermo-Calc software with the TCFE 12 database was employed to predict the volume fraction and chemical composition of austenite. These predicted compositions were used to calculate the martensite start temperature (M_s) and the stacking fault energy (γ_{SFE}) of the austenite phase.

Tensile tests were carried out on dog-bone specimens (25 mm in gauge length, 5 mm in diameter) using an MTS100 machine at a strain rate of 1×10^{-3} s^{-1}. After fracture, approximately 5 mm× 5 mm square sections were extracted from the fracture zone for post-deformation microstructural analysis. For corrosion resistance evaluation, specimens (50 mm×30 mm×5 mm) were immersed in a 6% $FeCl_3$-HCl solution at 50 °C for 24 h. Mass loss was determined by weighing the samples before and after immersion to calculate the corrosion rate. In addition, linear potentiodynamic polarization tests were performed in a 3.5wt.% NaCl solution at 25 °C (sweep rate: 0.5 mV·s^{-1}) using a Corrtest CS2350H electrochemical workstation.

3 Results

3.1 Microstructure of experimental steel under various treatments

Figure 2(a) illustrates the phase fractions of the experimental steel as a function of temperature under equilibrium conditions, omitting phases below 0.5% for clarity. Due to the extremely low carbon content, the martensite formed in the microstructure exhibits a body-centered cubic (BCC) structure. The presence of Mo and Si promotes the precipitation of the Laves phase at temperatures below 750 °C. The phase diagram indicates that under equilibrium conditions, δ-ferrite would fully transform into austenite at approximately 1,300 °C. However, owing to the high silicon content (~2.6wt.%), during the peritectic reaction (L+δ→γ) in the casting process, ferrite-stabilizing elements such as Si and Cr tend to enrich in both the liquid and δ-ferrite phases. This enrichment reduces the chemical driving force for the δ→γ transformation[21], leading to the retention of δ-ferrite from high-temperature states in the final microstructure, as observed in Fig. 3(a). Figure 2(b) presents a magnified view of the critical tempering temperature range (550–670 °C). As the temperature increases within this range, the predicted volume fraction of reverted austenite also rises, with the fraction of martensite and austenite approaching equal at around 610 °C.

Figure 3(a) shows a color metallographic image of the experimental steel after solution treatment at 1,050 °C, captured via optical microscopy. The bright regions correspond to δ-ferrite, with a volume fraction quantified at 11.7%. The remaining 88.3% is primarily martensite, within which a very small amount of retained austenite is also present. However, this austenite is embedded in the martensitic matrix and cannot be clearly distinguished from martensite under optical microscopy. Figure 3(b) presents the band contrast map and phase map of the S1050 specimen. δ-ferrite appears as elongated structures tens of micrometers long or as ~10 μm granular features around martensite. The martensite exhibits a lath morphology with widths typically in the range of a few micrometers. Small amounts (<1%) of residual austenite (red regions) are found between the martensitic laths. Figures 3(c)–(e) display the microstructures of the ST

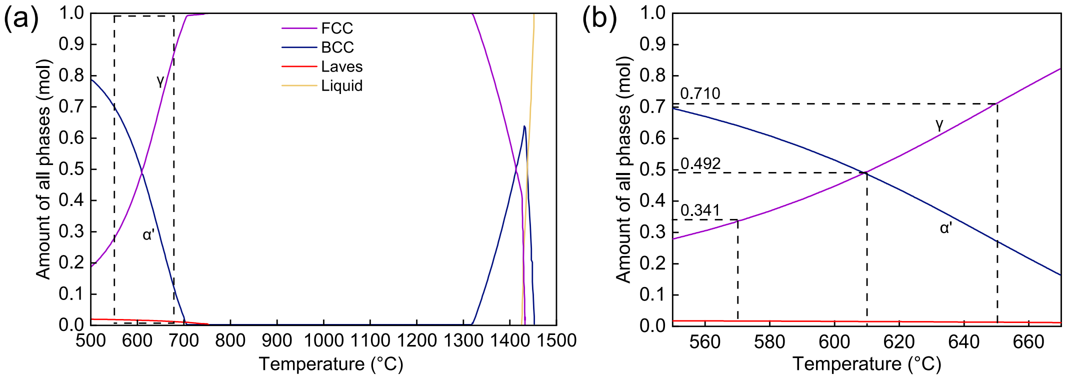

Fig. 2: Calculated equilibrium phase diagram of the experimental steel by Thermo-Calc software (a) and close-up view of (a) (b) (γ: austenite; α′: martensite)

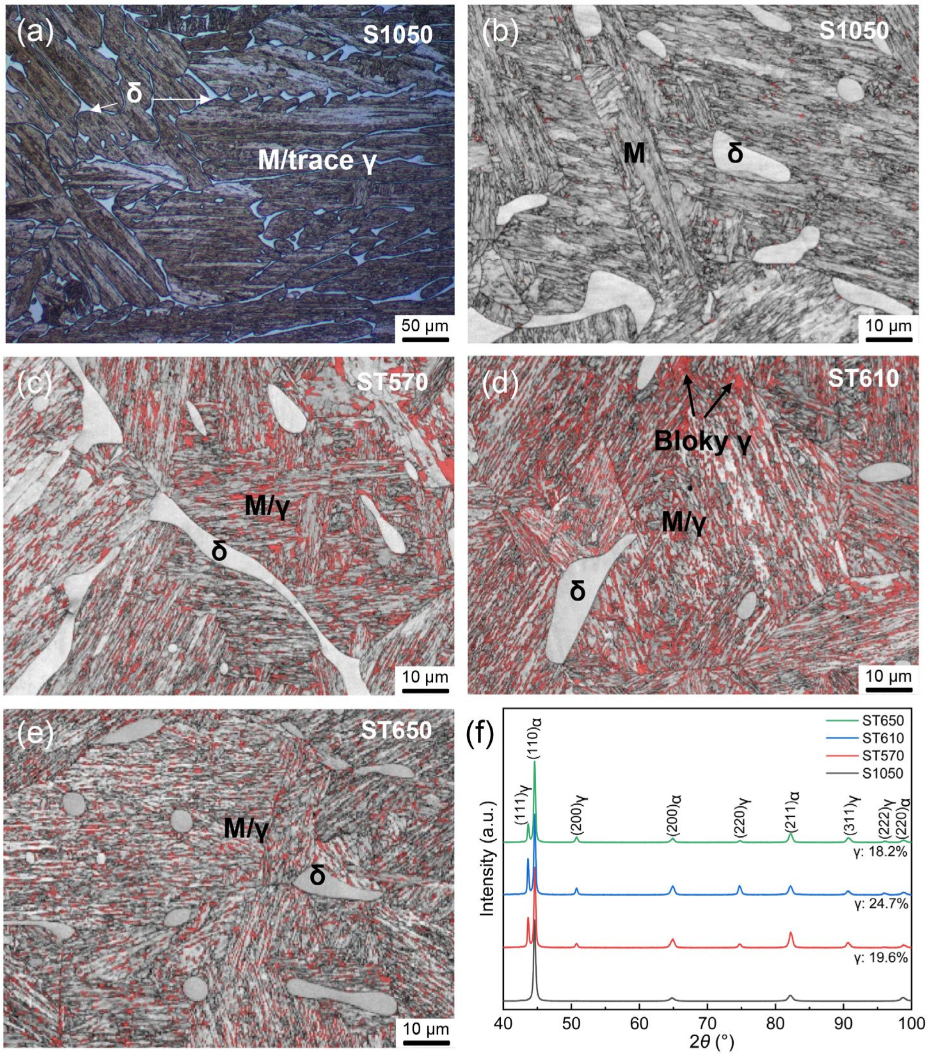

Fig. 3: Color metallography of S1050 (a), band contrast (BC) maps and phase maps for S1050 (b), ST570 (c), ST610 (d), and ST650 (e), and XRD profiles of all specimens (f) [δ-ferrite; M-martensite; γ-austenite (red region)]

specimens. Upon tempering, the martensitic laths become significantly finer, while δ-ferrite distribution remains similar to that in S1050. A key difference is the significant formation of reverted austenite between martensite laths in the ST specimens. The geometric mean size of reverted austenite grains, measured using AztecCrystal and calculated, reaches 1.06 μm for ST570, 1.04 μm for ST610, and 0.99 μm for ST650. Additionally, ST570 and ST610 exhibit more blocky austenite than ST650, though ST570 has a lower overall austenite density than the other two.

Figure 3(f) presents the XRD profiles of all the specimens. No diffraction peaks corresponding to the austenite phase are detected in the S1050 specimen, indicating that the residual austenite content after solution treatment is extremely low and below the detection limit. In contrast, distinct austenite peaks appear in the XRD patterns of the three critically tempered specimens. Austenite volume fractions are quantified via Rietveld refinement using Maud software, with all Rwp values, an indicator of fitting quality, below the 20% threshold recommended by Kisi[22]. Rwp reflects the agreement between calculated and experimental diffraction patterns. Austenite contents in the ST570, ST610, and ST650 specimens are found to be 19.6%, 24.7%, and 18.2%, respectively. Considering the equilibrium predictions shown in Fig. 2(b) at 570 °C, 610 °C, and 650 °C, it is evident that during cooling after critical tempering, a portion of the reverted austenite undergoes a secondary martensitic transformation. Moreover, as the tempering temperature increases, a larger fraction of the initially formed austenite reverts back to martensite. Therefore, the actual austenite content in the ST specimens initially increases and then decreases with increasing tempering temperature, deviating from the monotonic increase predicted under equilibrium conditions. Additionally, the austenite grains that undergo secondary transformation tend to coarsen before transforming, which explains the smaller average grain size and the reduced amount of blocky austenite observed in the ST650 specimen.

3.2 Mechanical properties

Figure 4(a) and Table 2 present the engineering stress-strain curves and mechanical properties of S1050, ST570, ST610, and ST650 specimens. All the specimens exhibit continuous yielding behavior. The yield strength (YS) of each specimen is determined using the 0.2% offset method per Chinese Standard GB/T 228.1-2021. For the S1050 specimen, the

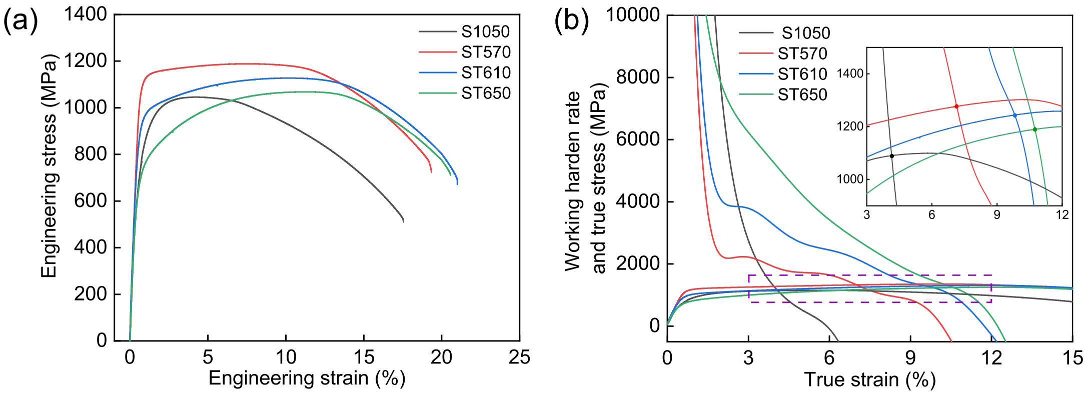

Fig. 4: Tensile stress-strain curves for S1050, ST570, ST610, and ST650 specimens: (a) engineering stress-strain curves; (b) true stress-strain and working hardening rate curves

Table 2: Mechanical properties of specimens with various treatment states

Specimens	YS (MPa)	UTS (MPa)	UE (%)	TE (%)	YR	PSE (GPa·%)
S1050	698±8	1,042±6	4.1±0.2	17.5±0.8	0.65	18.2
ST570	1,075±10	1,184±7	7.1±0.4	19.3±0.5	0.91	22.8
ST610	871±25	1,125±13	9.8±0.3	21.0±0.7	0.77	23.6
ST650	640±8	1,068±11	10.7±0.6	20.5±0.9	0.60	21.9

0.2% yield strength is approximately 698 MPa, and the ultimate tensile strength (UTS) reaches about 1,042 MPa. The yield ratio (YR, defined as YS/UTS) is calculated to be 0.65. This specimen exhibits the lowest uniform elongation (UE) and total elongation (TE), measured at approximately 4.1% and 17.5%, respectively. To comprehensively evaluate the mechanical performance, the product of UTS and TE (PSE) was calculated. The S1050 specimen demonstrates the lowest PSE value of 18.2 GPa·%, which is significantly lower than those of the ST series specimens (ranging from 21.9 to 23.6 GPa·%), highlighting the enhancement in the strength-ductility synergy achieved through critical tempering treatments.

After critical tempering treatment, the UE of the ST series specimens increases to approximately 7.1%, 9.8%, and 10.7%, respectively. The plasticity increases with the rise in tempering temperature, surpassing that of S1050 (~5.1%) by 40% to 100%. The reverse transformation of austenite during tempering plays a key role in enhancing plasticity. The YS of ST570 and ST610 increases to ~1,075 MPa and ~871 MPa, respectively, while the UTS improves to ~1,184 MPa and ~1,125 MPa, and the YR rises to 0.91 and 0.77. However, the YS of ST650 decreases to ~640 MPa, with the UTS at ~1,068 MPa, and the YR drops to 0.60. As the tempering temperature increases, the strength and the YR of the ST series specimens decrease. The ST610 specimen achieves the highest PSE value of 23.6 GPa·%, indicating the optimal strength-ductility balance among all the samples.

The working hardening rate (WHR) curve and true stress-strain curves are plotted in Fig. 4(b). The WHR curve is derived by differentiating every twenty data points on the true stress-strain curve to minimize noise. When the true strain (ε_T) is less than 2%, all specimens show a rapid WHR decrease due to the deformation of the soft phase (such as δ-ferrite or austenite) and dislocation movement[23]. For S1050, the WHR curve intersects the true stress curve at the necking point as ε_T increases. The ε_T value at this point is approximately 4.1%, which is equal to the value of UE[24]. For the ST series specimens, WHR increases with the rise in tempering temperature, and ε_T value at the necking point gradually increases, consistently exceeding that of the S1050 specimen. This is in agreement with the description of UE in Table 2, indicating that the ST series specimens exhibit better work hardening ability and higher toughness during the later stages of tensile deformation compared to the S1050 specimen. For ST570 and ST610, the decline in WHR noticeably decelerates at $\varepsilon_T \approx 2\%$, with the curve becoming relatively flat until necking. In ST650, this deceleration begins earlier in the tensile process and proceeds more gradually. The slower WHR reduction observed in the ST specimens is attributed to the TRIP effect induced by the reverted austenite[25]. Variations in the mechanical stability of austenite among the specimens lead to differences in the activation stages of the TRIP effect, which in turn influence the strength and tensile ductility of the materials[26].

3.3 Corrosion resistance performance test

To investigate the effect of tempering temperature on the corrosion resistance of the tested steel specimens, immersion and polarization curve tests were conducted, as shown in Fig. 5. In Fig. 5(a), the pitting corrosion pits formed on the surface of the tempered specimens are generally larger than those on the S1050 specimen. ST570 exhibits densely distributed pits smaller than 100 μm, whereas ST610 and ST650 show fewer but larger pits, ranging from 300 μm to 500 μm. As the tempering temperature increases, the diameter of the corrosion pits grows, while pit density initially decreases and then increases, indicating localized corrosion behavior. Figure 5(b) shows the polarization curves of the specimens in a 3.5wt.% NaCl solution. All the specimens exhibit a passivation region between the self-corrosion potential (E_{corr}) and the pitting potential (E_{pit}), where the corrosion current rate slows down, indicating that all the test steels possess some degree of corrosion resistance. S1050 shows the highest E_{corr} at -277 mV$_{SCE}$, while E_{corr} values for ST570, ST610, and ST650 are -307 mV$_{SCE}$, -318 mV$_{SCE}$, and -336 mV$_{SCE}$, respectively. The self-corrosion potential of the specimens decreases as the tempering temperature increases.

Figure 5(c) summarizes the weight loss rates and the ΔE_{pass} values of the specimens after the immersion test, as corresponding to Fig. 5(b). The weight loss rate (v_{wl}) is calculated according to Eq. (1), where m_0 and m_1 are the initial and final weights of the specimens, S is the surface area of the specimen, and t is the immersion time (24 h). ΔE_{pass} represents the difference between E_{pit} and E_{corr}, which reflects the width of the passivation region. It is a key indicator for evaluating the corrosion resistance of stainless steel[27].

$$v_{wl} = \frac{m_0 - m_1}{S \cdot t} \tag{1}$$

As shown in Fig. 5(c), after tempering treatment, the weight loss rate of the specimens increases from 19.1 g·(m^2·h)$^{-1}$ for the S1050 specimen to 35.5–38.5 g·(m^2·h)$^{-1}$, and the passivation region width (ΔE_{pass}) decreases from 480 mV$_{SCE}$ to 415–435 mV$_{SCE}$. This indicates that tempering treatment reduces the corrosion resistance of the test steels. As the tempering temperature increases, the weight loss rate of the specimens rises, and the passivation region width (ΔE_{pass}) decreases. Additionally, Fig. 5(a) reveals that after immersion, the pitting corrosion on ST650 exhibits larger pit diameters and a higher quantity of pits. These results suggest that excessively high tempering temperatures significantly impair the corrosion resistance of the steel.

4 Discussion

4.1 Stability of reverted austenite

The reverted austenite formed during the critical tempering of the experimental steel has a profound impact on its performance. Figure 6(a) presents the calculated chemical composition of the reverted austenite at different tempering temperatures. As the temperature increases, an enrichment of ferrite-stabilizing elements such as Cr and Si is observed, whereas the concentrations of austenite-stabilizing elements like Ni and Mn decrease. Austenite composition strongly influences its stability, including both thermal and mechanical aspects. Thermal stability determines the extent of martensitic transformation during cooling, whereas mechanical stability governs the degree of strain-induced transformation during tensile deformation.

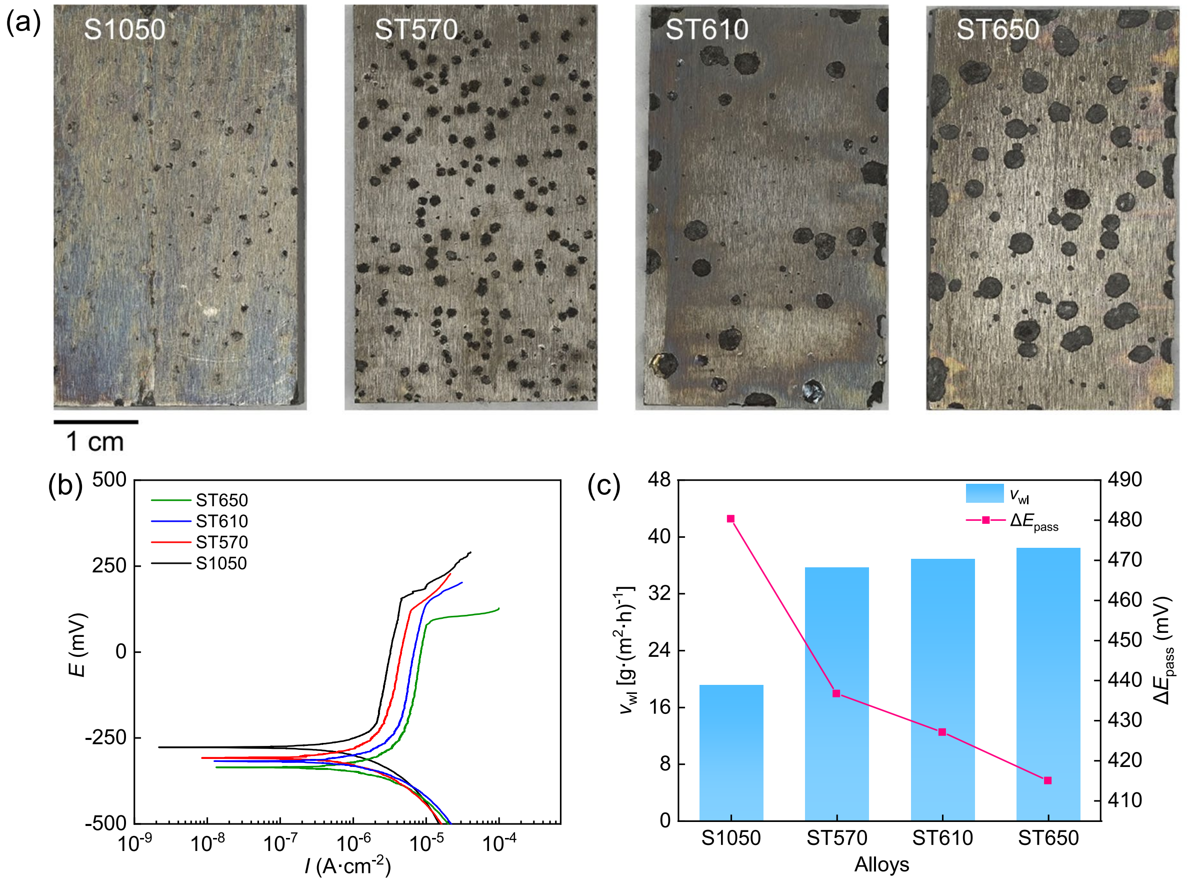

Fig. 5: Surface of specimens after being soaked in ferric chloride hydrochloric acid solution at 50 °C for 24 h (a), polarization curves of specimens in 3.5wt.% NaCl solution (b), the mass loss rate during immersion test and passivation region width of specimens (c)

In Fig. 2(b), the predicted equilibrium volume fraction of austenite increases with the rise in tempering temperature, from 34% at 570 °C to 71% at 650 °C. However, this significantly exceeds the actual austenite contents measured by XRD in the ST specimens (18%–25%), due to partial retransformation of the reversed-transformed austenite into martensite during post-tempering cooling. The retained austenite fraction measured by XRD reflects the final state after cooling. Figure 6(b) compares the predicted equilibrium fractions with the experimentally measured values. At 570 °C, approximately 53% of the austenite is retained after cooling (decreasing from 34.1% to 18.2%). This retention increases to 59% at 610 °C but drops markedly to 28% at 650 °C, indicating that a higher tempering temperature promotes secondary martensitic transformation. Additionally, based on the compositional data in Fig. 6(a), the M_s temperature of the austenite at different tempering temperatures was calculated using the empirical equation proposed by Barbier[28]:

$$\begin{aligned} M_s = {} & 545 - 601.2 \times [1 - \exp(1 - 0.868\mathrm{C})] - \\ & 34.4\mathrm{Mn} - 13.7\mathrm{Si} - 9.2\mathrm{Cr} - 17.3\mathrm{Ni} - \\ & 15.4\mathrm{Mo} + 10.8\mathrm{V} + 4.7\mathrm{Co} - 1.4\mathrm{Al} - \\ & 16.3\mathrm{Cu} - 361\mathrm{Nb} - 2.44\mathrm{Ti} - 3448\mathrm{B} \end{aligned} \tag{2}$$

The M_s temperature increases with rising tempering temperature, indicating that the thermal stability of austenite decreases as a result of elemental partitioning at higher tempering temperatures, as shown in Fig. 6(b). Consequently, reverted austenite formed at elevated temperatures becomes more susceptible to martensitic transformation during subsequent cooling. As a result, the retained austenite content in the final microstructure does not vary monotonically with tempering temperature. This phenomenon also explains why the highest austenite content after critical tempering is achieved at 610 °C.

The tensile ductility and strength of martensitic stainless steels containing austenite are significantly affected by specific deformation mechanisms, notably the TRIP and TWIP effect. Both mechanisms involve phase transformation or structural evolution of the austenite phase under applied stress or strain and are primarily determined by the mechanical stability of austenite. As a face-centered cubic (FCC) phase, the deformation behavior and mechanical properties of austenite are strongly dependent on its stacking fault energy (γ_{SFE})[29]. Accordingly, the mechanical stability of austenite can be assessed by calculating its γ_{SFE} value, based on the classical Olson-Cohen thermodynamic model[30, 31]:

$$\gamma_{\mathrm{SFE}} = 2\rho\Delta G^{\gamma\to\varepsilon} + 2v \tag{3}$$

$$\rho = \frac{4}{\sqrt{3}} \cdot \frac{1}{a^2 N_{\mathrm{A}}} \tag{4}$$

where, ρ denotes the molar surface density of the (111) plane, calculated as 2.96×10^{-5} mol·m^{-2} based on Eq. (4), a is the lattice parameter of austenite (3.60 Å) and N_{A} is Avogadro's number. The parameter v, representing the FCC/HCP interfacial

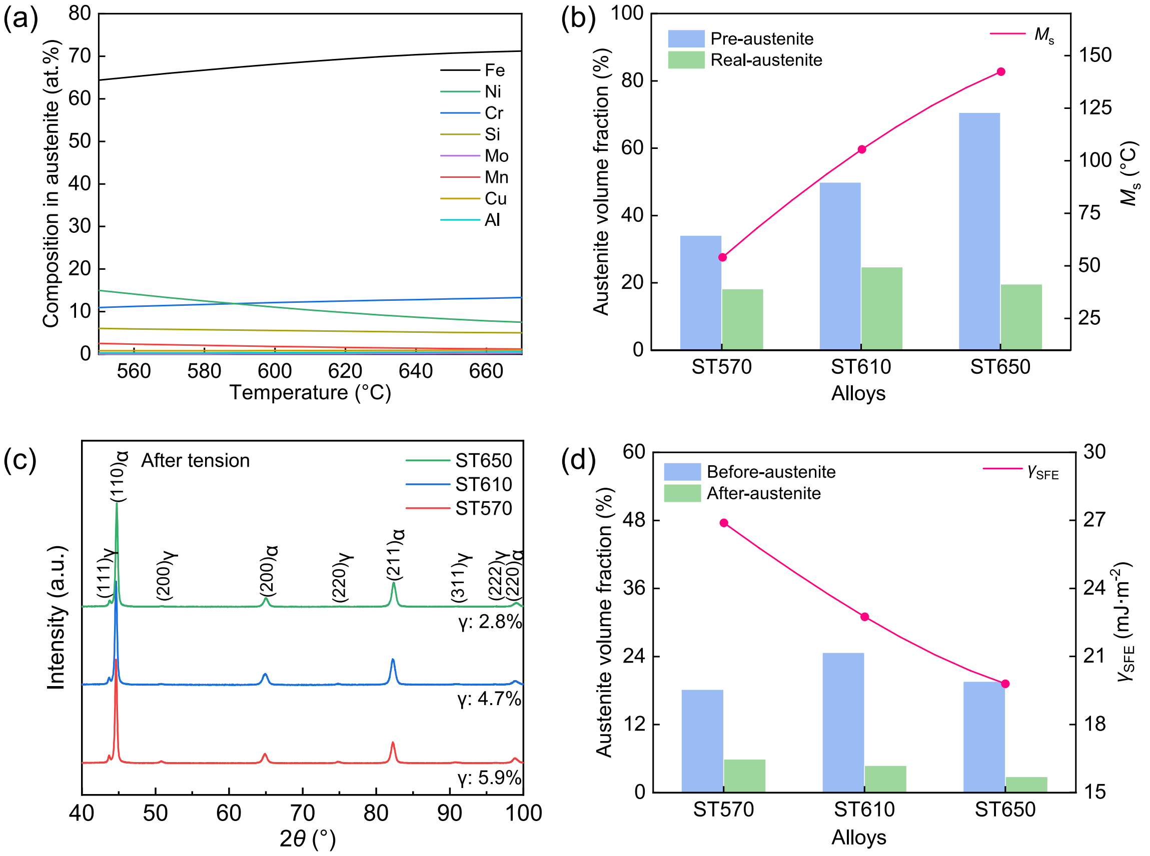

Fig. 6: Calculated composition of reverted austenite vs. tempering temperature (a), M_s temperature calculated from (a) with predicted and measured austenite fractions of ST specimens (b), XRD profiles of ST specimens after tensile testing (c), and SFE calculated from (a) with measured austenite fractions before and after testing (d)

energy, is estimated to be ~8 mJ·m^{-2} from recent *ab initio* calculations in the Fe-Cr-Ni system[32]. $\Delta G^{\gamma\rightarrow\varepsilon}$ refers to the driving force for the phase transformation from austenite to ε-martensite, which is determined by the chemical composition of the austenite. The driving force can be calculated based on the elemental compositions shown in Fig. 6(a), following the methodology proposed by Curtze et al[33].

Figure 6(c) presents the XRD profiles of the ST specimens after tensile testing, with austenite fractions quantified via Rietveld refinement using Maud software. Figure 6(d) illustrates the changes in austenite content before and after deformation. All ST specimens exhibit a marked reduction in austenite content (less than 6% remaining), indicating significant TRIP effects during deformation, which contributes to improved tensile ductility. The fraction of austenite transformed during tensile deformation varies among the ST specimens: approximately 69% of austenite transformed in ST570, while higher transformation ratios of 81% and 86% are observed in ST610 and ST650, respectively. This suggests that the austenite in ST570 exhibits the highest mechanical stability. The calculated γ_{SFE} values show a consistent trend, decreasing from 27 mJ·m^{-2} to 20 mJ·m^{-2} across the ST specimens, attributable to variations in the chemical composition of the austenite phase. According to established criteria, austenite with γ_{SFE} below ~20 mJ·m^{-2} tends to transform via TRIP, 20–40 mJ·m^{-2} corresponds to a mixed TRIP/TWIP regime, and values above ~40 mJ·m^{-2} favor TWIP-dominated behavior[34]. Given that the ST specimens fall within the 20–27 mJ·m^{-2} range, their austenite is expected to undergo both TRIP and TWIP. In particular, ST570, with the highest γ_{SFE}, likely experienced contributions from both mechanisms, whereas ST650, with the lowest γ_{SFE}, is mainly governed by TRIP, consistent with its larger fraction of deformation-induced transformation. The lower mechanical stability of austenite in ST650 also explains its earlier transformation during tensile loading, which promotes premature yielding and consequently reduced yield strength[35].

4.2 Microstructure evolution and deformation mechanisms

The multiple phase transformations occurring during the critical tempering process significantly influence the final microstructure of the specimens, thereby influencing their overall performance. The formation of reverted austenite and the subsequent transformation of unstable austenite during tempering affect the dislocation structure and grain boundary density within the microstructure. Figure 7 presents the KAM maps and GB distribution maps for the S1050 and the ST series specimens at various tempering temperatures. The geometrically necessary dislocations (GND) in the specimens can be calculated using Eq. (5), where μ is the EBSD step size for each map, fixed at 0.176 μm, b is the magnitude of the Burgers vector for BCC iron, taken as 0.248 nm, and KAM$_{\text{ave}}$ represents the geometric mean of the KAM values of the pixels within the statistical region, minimizing the influence of outlier values[36, 37]. KAM$_{\text{ave}}$ values for five martensite and ferrite regions in the microstructure were computed to determine the corresponding GND densities (ρ_{GND}), as shown in Fig. 8(a). Figure 8(b) presents the grain boundary density at various misorientation angles for each specimen. The grain boundary density was calculated as the ratio of the length of grain boundaries at a given misorientation angle to the area of the measured region.

$$\rho_{\text{GND}} = 2\text{KAM}_{\text{ave}}/\mu b \tag{5}$$

There is a clear difference in GND density between the ferrite and martensite phases across all the specimens. Ferrite exhibits a much lower dislocation density than martensite, indicating it is the softer phase, while the strength is primarily provided by martensite. The dislocation density in ferrite remains relatively unaffected by tempering treatments, whereas more pronounced changes occur in the martensite phase. The higher dislocation density in S1050 corresponds to higher strength and lower tensile ductility, which can be attributed to stress concentration during the tensile deformation. In contrast, precipitation phases and reverted austenite formed during tempering in the ST specimens have a more significant effect on both strength and ductility, leading to improved mechanical performance. As the tempering temperature increases, the dislocation density initially decreases and then increases. The prevailing view is that recovery during tempering leads to the annihilation of dislocations with opposite signs, thereby reducing dislocation density. However, the abnormal increase in dislocation density observed in ST650 martensite is likely due to the formation of secondary martensite from unstable austenite, which introduces additional dislocations and outweighs the effect of recovery. Compared to the higher GND density in S1050, the lower GND density in the ST specimens facilitates more coordinated deformation between martensite and ferrite. The anomalous increase in dislocation density in ST650 contributes to its reduced ductility relative to ST610[38].

Figure 8(b) shows the grain boundary density distribution for all the specimens. The grain boundaries are categorized into three groups according to their interface angle: 5°–10°, 10°–45°, and >45°, with boundaries greater than 10° classified as high-angle grain boundaries, which are generally associated with improved strength but reduced ductility[39]. The overall trend in grain boundary density follows the same pattern as the GND density, reflecting the synergistic effect of tempering treatment on dislocation and grain boundary densities. Boundaries between ferrite and martensite are mostly in the 10°–45° range, while >45° boundaries are prevalent between martensite-based laths. The influence of grain boundaries on mechanical behavior is primarily mediated through their effect on the martensitic phase. In ST650, the density of high-angle boundaries increases due to secondary martensite formation; however, this does not substantially enhance strength. Therefore, it can be concluded that neither dislocation strengthening nor grain boundary strengthening plays a dominant role in determining the yield strength of the ST specimens.

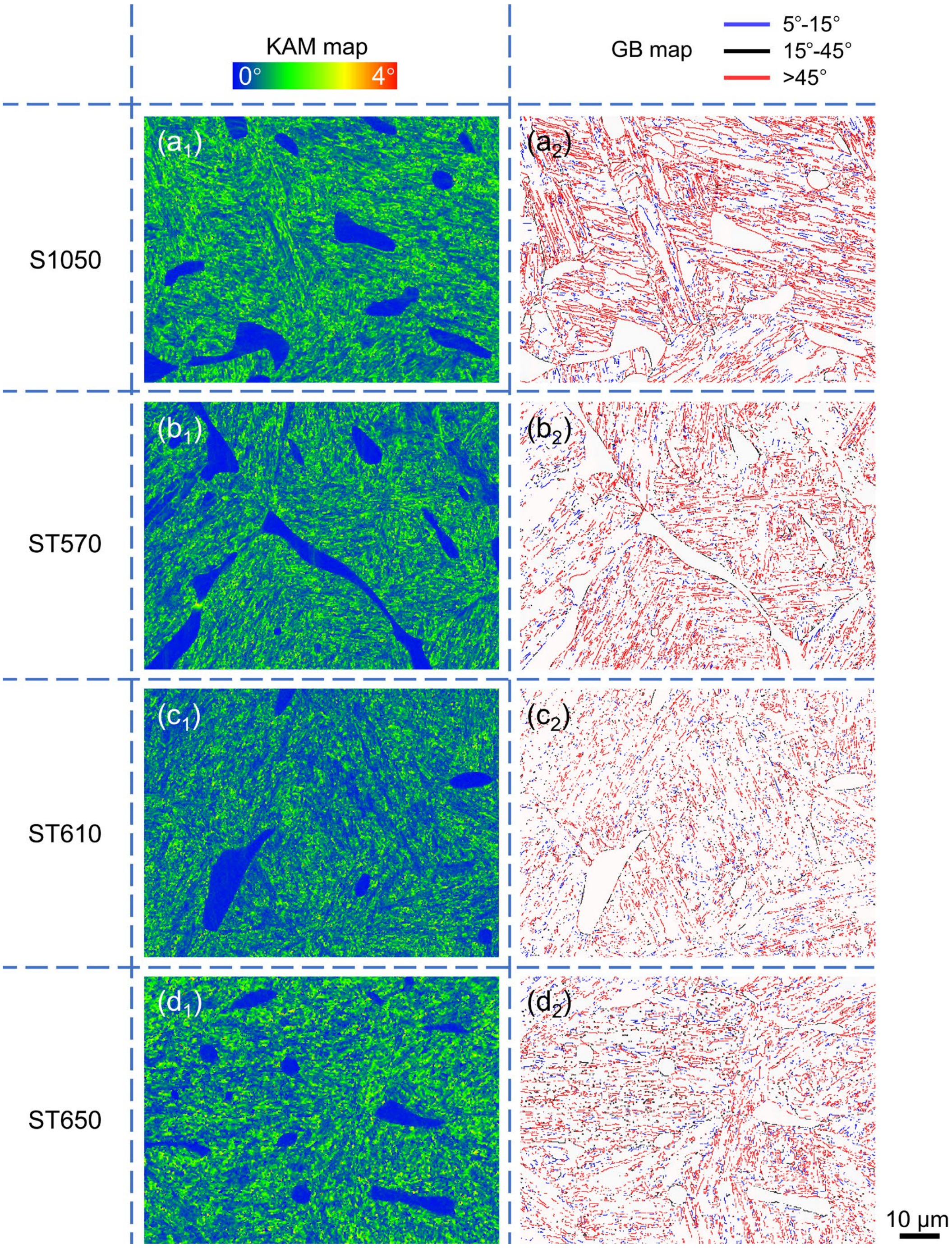

Fig. 7: KAM maps (a_1, b_1, c_1, d_1) and GB distribution maps (a_2, b_2, c_2, d_2) for S1050, ST570, ST610, and ST650 specimens

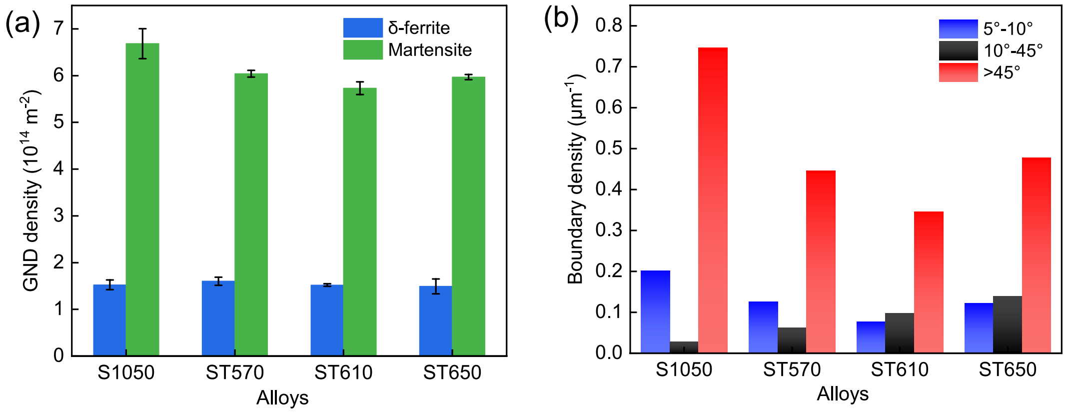

Fig. 8: GND density (a) and grain boundary density (b) of specimens corresponding to Fig. 7

The increase in yield strength of ST570 compared to S1050 is primarily attributed to the formation of Laves phases[40, 41] and nanoscale austenite phases[26] within the microstructure. Precipitation hardening contributes more to strength enhancement than dislocation or grain boundary strengthening. Figure 9 shows bright-field TEM images of various phases in the ST570 specimen after tensile testing. In Fig. 9(a), Laves phase precipitates, typically tens of nanometers in size, are observed within the martensitic matrix. Dislocations are entangled around these precipitates, which impede further dislocation motion and play a crucial role in increasing the yield strength. As shown in Fig. 2, the volume fraction of Laves phase is less than 3% and decreases with increasing tempering temperature, consistent with the trend of yield strength variation. Figure 9(b) shows the deformed ferrite phase, which initially has a lower dislocation density than martensite, resulting in fewer nucleation sites for precipitates; hence, no precipitates are observed. As the softer phase, ferrite mainly accommodates strain during tensile deformation, leading to dislocation accumulation near phase boundaries. These accumulated dislocations generate back stress, which hardens the ferrite and alleviates strain incompatibility and stress concentration between soft and hard phases, thereby contributing to overall mechanical performance[8, 42]. Figures 9(c, d) illustrate the behavior of austenite during deformation. As previously discussed, austenite transforms into martensite via the TRIP effect. Figure 9(c) shows the Kurdjumov-Sachs (K-S) orientation relationship between austenite and strain-induced martensite, observed in a high-dislocation-density region, indicating that localized stress concentration triggered the transformation. Figure 9(d) reveals another deformation feature in the austenite phase [confirmed by selected area electron diffraction (SAED)] where nanoscale twinning bands, tens of nanometers wide, form perpendicular to the phase boundary. This observation suggests the occurrence of the TWIP effect in reverted austenite. Strain-induced twinning reduces the effective dislocation slip distance and alters grain orientation, promoting coordinated deformation and thereby enhancing both strength and ductility[43, 44].

As illustrated in Fig. 10, the deformation mechanism of the ST570 specimen steel during the tensile test was discussed. Prior to deformation [Fig. 10(a)], the microstructure consists of softer ferrite with low GND density and harder lath regions with high GND density, where reverted austenite and precipitates are distributed within a martensitic matrix. During tensile loading [Fig. 10(b)], the GND density between martensitic laths increases significantly, indicating strain concentration in these regions. This triggers the synergistic activation of TRIP and TWIP effects in the inter-lath austenite, thereby enhancing strain accommodation. Notably, this cooperative deformation mechanism occurs earlier in the ST650 specimen and contributes to its premature yielding. Simultaneously, dislocations in the ferrite phase are activated and accumulate at phase boundaries, generating back stress that helps relieve stress concentration. At the necking stage [Fig. 10(c)], dislocations continue to accumulate between martensitic laths, while most of the reverted austenites are transformed due to ongoing TRIP effects. In ferrite, dislocations gather at grain boundary regions, forming subgrain boundaries. These subgrains may rotate, further promoting strain compatibility and delaying crack initiation. Ultimately, cracks nucleate in GND-rich martensitic regions and at ferrite-martensite interfaces, leading to final fracture.

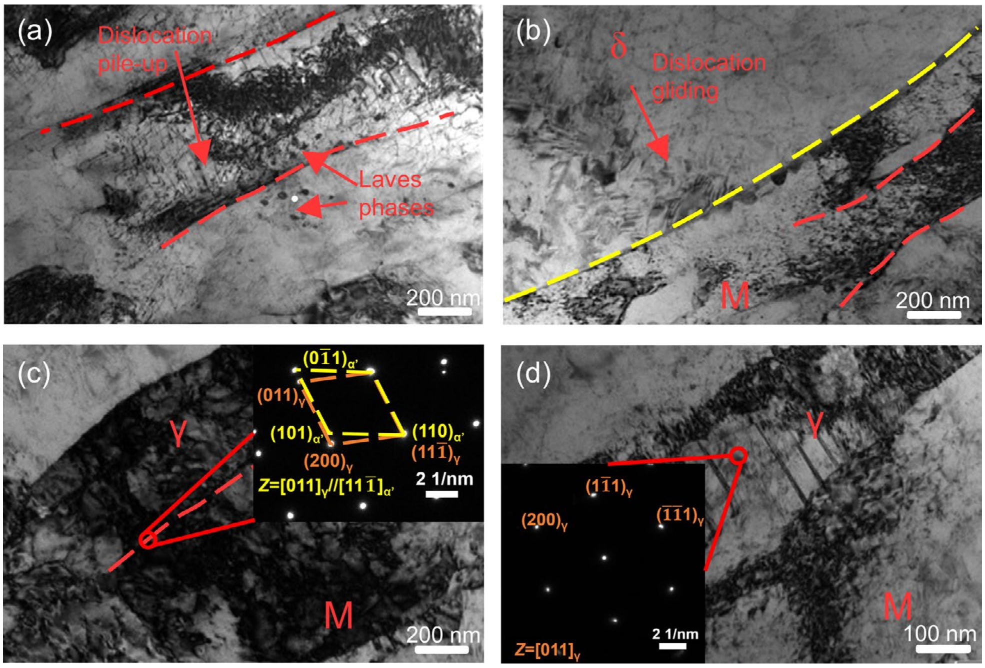

Fig. 9: Bright-field TEM images of ST570 after tensile testing: (a) martensite with nanoscale Laves phase precipitates and entangled dislocations; (b) ferrite showing dislocation accumulation near phase boundaries; (c) austenite transforming into martensite via TRIP effect, with K-S relationship; (d) reverted austenite with nanoscale deformation twins, indicating the TWIP effect

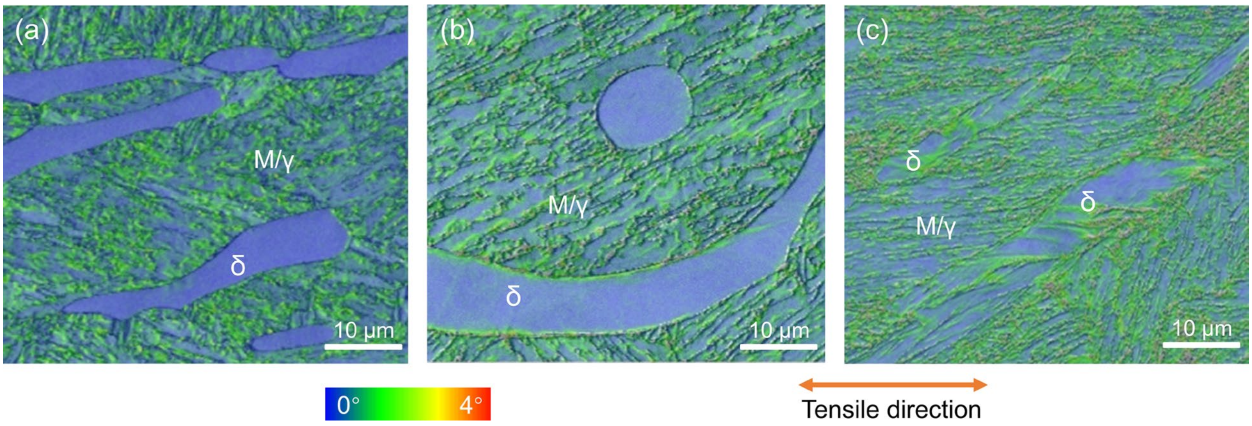

Fig. 10: Band contrast maps and KAM maps for ST570 specimens before tensile test (a), at yield (b), and at necking (c)

4.3 Cr inhomogeneity accelerates corrosion

Figure 11 shows SEM images of micron-scale corrosion pits in the ST570 specimen. These corrosion pits appear at the martensite/austenite composite (M+γ) laths and phase boundaries, while no corrosion damage is observed within the ferrite (δ) phase. Figure 11(b) provides a magnified view of corrosion at a phase boundary, where pits propagate along the interface, leading to selective dissolution of the martensite phase, while the ferrite remains largely unaffected. Chromium (Cr), a key element in enhancing corrosion resistance, contributes to the formation of a protective passive film on stainless steel surfaces[45-47]. Figures 12(a$_1$, b$_1$) show EBSD band contrast maps of the ST570 and ST650 specimens, with red lines traversing M+γ and δ regions. Chromium concentration along these lines was analyzed via SEM-EDS. A low-pass FFT filter with a DC offset (f<1/7 μm^{-1}) was applied to the concentration profile to reduce noise, as shown in Figs. 12(a$_2$, b$_2$). The Cr concentration exhibits vatiation within 10wt.%–18wt.%, with its fluctuation pattern corresponding to the M+γ and δ distribution in the microstructure. Chromium is enriched in the δ phase and depleted in the M+γ laths, with significant concentration changes at phase boundaries and smaller variations within each phase. Comparatively, the composition fluctuations in ST650 are significantly greater than those in ST570. A distinct Cr-depleted zone is observed at the phase boundary in ST650, where lower and more uneven Cr content is attributed to the enhanced Cr diffusion at higher tempering temperatures.

The Cr content at different microstructural locations affects both the thickness and quality of the passive film, which is primarily composed of Cr and Fe oxides. A thicker and less defective passive film offers better resistance to dissolution during corrosion[48, 49]. The passive film formed on the M+γ lath surface is more susceptible to breakdown, particularly in Cr-depleted regions near phase boundaries. As pitting corrosion initiates, cavities first develop within the M+γ laths or at phase boundaries and then expand further within the laths. Once the M+γ surrounding a ferrite grain is fully corroded, the ferrite grain may detach, leading to further enlargement of the pits. From an electrochemical standpoint, according to the Cr-depletion theory, Cr-depleted regions act as micro-anodes and undergo preferential dissolution, while Cr-rich regions serve as micro-cathodes and are relatively protected[50]. This micro-galvanic coupling accelerates the dissolution of M+γ laths, particularly at phase boundaries. As the tempering temperature increases, the passive film quality in Cr-depleted boundaries deteriorates, raising the corrosion loop potential and further accelerating matrix dissolution near these boundaries. Ferrite grains become more easily detached, resulting in larger corrosion pits, as observed in Fig. 5(a) for the ST650 specimen. Consequently, the corrosion resistance of the ST specimens, indicated by a reduction in the passivation width (ΔE_{pass}) and an increase in v_{wl}, decreases as the tempering temperature increases.

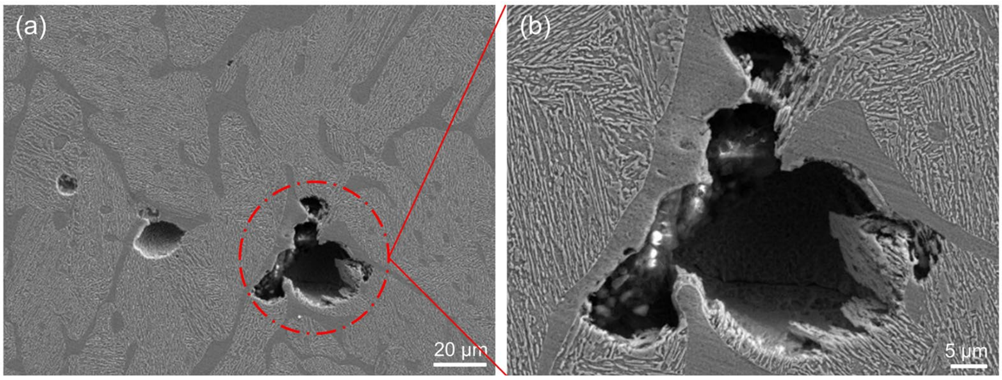

Fig. 11: SEM images of ST570 specimen surface after immersion corrosion test (a–b)

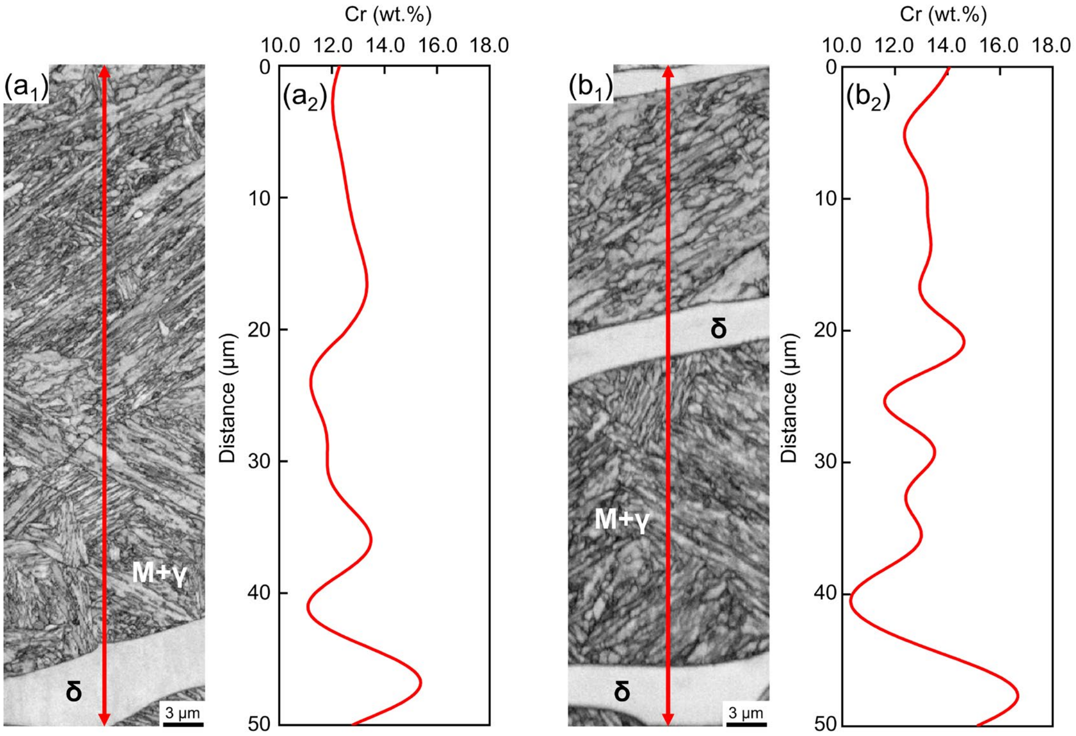

Fig. 12: EBSD maps of ST570 specimen (a$_1$) and ST650 specimen (b$_1$), Cr concentration profile of ST570 specimen (a$_2$) and ST650 specimen (b$_2$) after applying a low pass FFT filter (f<1/7 μm^{-1}) along the red lines in (a$_1$) and (b$_1$)

5 Conclusions

In this work, the effects of critical tempering on the phase evolution and properties of a novel cast multiphase stainless steel [Fe-13.5Cr-2.6Si-6.9Ni-1.1Cu-1.1Mn-1.0Mo-0.35Al-0.025C (wt.%)] were systematically investigated. Particular emphasis is placed on the stability of reverted austenite, which is found to play a decisive role in governing the balance between strength and ductility. Notably, the study reveals that the corrosion resistance of triphase stainless steel deteriorates significantly after tempering, due to Cr segregation and chemical inhomogeneity at phase boundaries. The major findings are summarized as follows:

(1) After solution treatment at 1,050 °C, the steel exhibits a multiphase microstructure consisting of approximately 11.7% δ-ferrite and 88.3% martensite with trace austenite. Critical tempering treatments between 570 °C and 650 °C induce significant formation of reverted austenite. The reverted austenite volume fraction firstly increases and then decreases with tempering temperature, reaching a maximum at 610 °C, before declining at 650 °C due to thermal instability and secondary martensitic transformation upon cooling.

(2) The stability of reverted austenite plays a pivotal role in determining mechanical behavior. Lower γ_{SFE}, resulting from compositional changes during tempering, enhances the TRIP effect, thereby improving ductility at the expense of yield strength. The mechanical stability of reverted austenite is temperature-dependent, with optimal stability observed at moderate tempering temperatures (610 °C), leading to balanced strength and toughness.

(3) The mechanical behavior is notably enhanced through critical tempering. The ST610 specimen demonstrates superior performance, achieving a YS of ~871 MPa, an UTS of ~1,125 MPa, and a TE of ~21.0%, culminating in the highest PSE of ~23.6 GPa·%. This remarkable strength-ductility synergy is attributed to a combination of strengthening mechanisms, including fine laves phase precipitation, stress-induced martensitic transformation (TRIP effect), deformation twinning (TWIP effect), and back-stress hardening arising from heterogeneous microstructures.

(4) Although mechanical properties improve, corrosion resistance deteriorates with increased tempering temperatures. Elevated temperatures promote Cr segregation at phase boundaries, resulting in the formation of Cr-depleted regions within the multiphase microstructure. These zones act as preferential sites for localized corrosion initiation, accelerating pit growth, and leading to increased weight loss rates and narrower passivation regions. Especially at 650 °C, extensive Cr inhomogeneity further exacerbates the corrosion susceptibility.

Acknowledgment

This work was supported by the Project of Science and Technology Cooperation of Inner Mongolia Autonomous Region of China (Grant No. 2022YFXM0008).

Conflict of interest

The authors declare that they have no known competing financial interests or personal relationships that could have appeared to influence the work reported in this paper.

References

[1] Wang C, Chang Y, Zhou F, et al. M^3 microstructure control theory and technology of the third-generation automotive steels with highstrength and high ductility. Acta Metall. Sin., 2020, 56(4): 400–410. https://doi.org/10.11900/0412.1961.2019.00371. (In Chinese)

[2] Tavares S S M, de Sampaio M T G, Perez G, et al. DL-EPR and AFM study of sensitization of a 17%Cr multiphase stainless steel. Mater. Corros., 2022, 73(6): 866–875. https://doi.org/10.1002/maco.202112814.

[3] Tavares S S M, Bastos I N, Pardal J M, et al. Slow strain rate tensile test results of new multiphase 17%Cr stainless steel under hydrogen cathodic charging. Int. J. Hydrogen Energy, 2015, 40(47): 16992–16999. https://doi.org/10.1016/j.ijhydene.2015.05.148.

[4] Liu M, Du C, Hai C, et al. Influence of Nb on the hydrogen-assisted cracking behaviour in multiphase stainless steel: Phase fractions, stacking fault energies, and nanosized NbC precipitation. Mater. Sci. Eng. A, 2024, 903: 146647. https://doi.org/10.1016/j.msea.2024.146647.

[5] Liu M, Huang S, Liu Z, et al. Investigations on the passive and pitting behaviors of the multiphase stainless steel in chlorine atmosphere. J. Mater. Res. Technol., 2024, 28: 3365–3375. https://doi.org/10.1016/j.jmrt.2023.12.243.

[6] Wu Z, Wang M, He J, et al. A novel cast multiphase stainless steel with high strength and high toughness. Metall. Mater. Trans. A, 2023, 54(7): 2617–2630. https://doi.org/10.1007/s11661-023-07039-3.

[7] Wu Z, Liu Y, Zhang H, et al. Microstructure and mechanical properties of a novel cast multi-phase stainless steel. J. Mater. Res. Technol., 2022, 19: 4177–4182. https://doi.org/10.1016/j.jmrt.2022.06.138.

[8] Wu Z, Wang M, He J, et al. Strain partitioning in ferrite and mechanical properties of a cast multiphase stainless steel. Mater. Today Commun., 2023, 35: 105644. https://doi.org/10.1016/j.mtcomm.2023.105644.

[9] Setia P, Venkateswaran T, Tharian K T, et al. Influence of Si content on the microstructure and mechanical properties of silicon stainless steel. Mater. Sci. Eng. A, 2022, 829: 142141. https://doi.org/10.1016/j.msea.2021.142141.

[10] Lee C, Roh S, Lee C, et al. Influence of Si on sigma phase precipitation and pitting corrosion in superaustenitic stainless steel weld metal. Mater. Chem. Phys., 2018, 207: 91–97. https://doi.org/10.1016/j.matchemphys.2017.12.055.

[11] Wilde B E. The influence of silicon on the pitting corrosion resistance of an 18Cr-8Ni stainless steel. Corrosion, 1986, 42(3): 147–151. https://doi.org/10.5006/1.3584894.

[12] Wang M X, Wu Z X, He J Y, et al. Microstructure and mechanical properties of a cast TRIP-assisted multiphase stainless steel. China Foundry, 2024, 21(3): 221–228. https://doi.org/10.1007/s41230-024-3080-3.

[13] Hamada A, Juuti T, Khosravifard A, et al. Effect of silicon on the hot deformation behavior of microalloyed TWIP-type stainless steels. Mater. Des., 2018, 154: 117–129. https://doi.org/10.1016/j.matdes.2018.05.029.

[14] Li J, Zhang Y, Jiang W, et al. Enhancing work hardening through tuning TRIP by nano-precipitates in maraging stainless steels. Int. J. Plast., 2025, 186: 104265. https://doi.org/10.1016/j.ijplas.2025.104265.

[15] Xiong X, He J, Zhi H, et al. Optimizing mechanical properties of 15Cr supermartensitic stainless steel by enhanced stability of retained austenite. Mater. Sci. Eng. A, 2022, 853: 143732. https://doi.org/10.1016/j.msea.2022.143732.

[16] He C, Xiao G, Hui P, et al. The new design to improve the stability of retained austenite and mechanical properties in super martensitic stainless steel. Mater. Charact., 2024, 217: 114342. https://doi.org/10.1016/j.matchar.2024.114342.

[17] Zhao Y, Zhu Z, Zhao X, et al. Clarify the effect of reversed austenite on the pitting corrosion resistance of super 13Cr martensitic stainless steel. Corros. Sci., 2023, 213: 110992. https://doi.org/10.1016/j.corsci.2023.110992.

[18] Wang P, Zheng W, Dai X, et al. Prominent role of reversed austenite on corrosion property of super 13Cr martensitic stainless steel. J. Mater. Res. Technol., 2023, 22: 1753–1767. https://doi.org/10.1016/j.jmrt.2022.12.016.

[19] Kim S H, Moon H K, Kang T, et al. Dissolution kinetics of delta ferrite in AISI 304 stainless steel produced by strip casting process. Mater. Sci. Eng. A, 2003, 356(1–2): 390–398. https://doi.org/10.1016/S0921-5093(03)00152-7.

[20] Lichtenegger P, Bloch R. Colour etching of high alloy steels. Pract. Metallogr., 1975, 12(11): 567–573. https://doi.org/10.1515/pm-1975-121101.

[21] Van Gen Hassend F, Weber S. Influence of chemical inhomogeneities on local phase stabilities and material properties in cast martensitic stainless steel. Steel Res. Int., 2020, 91(5): 1900481. https://doi.org/10.1002/srin.201900481.

[22] Kisi E H. Rietveld analysis of powder diffraction patterns. Mater. Forum, 1994, 18: 135–155.

[23] Lee S, Shin S, Kwon M, et al. Tensile properties of medium Mn steel with a bimodal UFG α+γ and coarse δ-ferrite microstructure. Metall. Mater. Trans. A, 2017, 48(4): 1678–1700. https://doi.org/10.1007/s11661-017-3979-z.

[24] Zhu Y, Wu X. Heterostructured materials. Prog. Mater. Sci., 2023, 131: 101019. https://doi.org/10.1016/j.pmatsci.2022.101019.

[25] Wang M M, Tasan C C, Ponge D, et al. Spectral TRIP enables ductile 1.1 GPa martensite. Acta Mater., 2016, 111: 262–272. https://doi.org/10.1016/j.actamat.2016.03.070.

[26] Oh H S, Kang J, Jiang M, et al. Role of the nanoscale austenite in micro-strain heterogeneity in PH17-4 martensitic stainless steels. Mater. Sci. Eng. A, 2024, 895: 146122. https://doi.org/10.1016/j.msea.2024.146122.

[27] Wang Z, Feng Z, Zhang L. Effect of high temperature on the corrosion behavior and passive film composition of 316 L stainless steel in high H_2S-containing environments. Corros. Sci., 2020, 174: 108844. https://doi.org/10.1016/j.corsci.2020.108844.

[28] Barbier D. Extension of the martensite transformation temperature relation to larger alloying elements and contents. Adv. Eng. Mater., 2014, 16(1): 122–127. https://doi.org/10.1002/adem.201300116.

[29] van der Wegen G J L, Bronsveld P M, de Hosson J Th M. A comparison between different theories predicting the stacking fault energy from extended nodes. Scr. Metall., 1980, 14(2): 285–288. https://doi.org/10.1016/0036-9748(80)90110-6.

[30] Olson G B, Cohen M. Kinetics of strain-induced martensitic nucleation. Metall. Trans. A, 1975, 6(4): 791–795. https://doi.org/10.1007/BF02672301.

[31] Olson G B, Cohen M. A mechanism for the strain-induced nucleation of martensitic transformations. J. Common Met., 1972, 28(1): 107–118. https://doi.org/10.1016/0022-5088(72)90173-7.

[32] Li R, Lu S, Kim D, et al. Stacking fault energy of face-centered cubic metals: Thermodynamic and *ab initio* approaches. J. Phys. Condens. Matter, 2016, 28(39): 395001. https://doi.org/10.1088/0953-8984/28/39/395001.

[33] Curtze S, Kuokkala V T. Dependence of tensile deformation behavior of TWIP steels on stacking fault energy, temperature and strain rate. Acta Mater., 2010, 58(15): 5129–5141. https://doi.org/10.1016/j.actamat.2010.05.049.

[34] Lee Y K, Lee S J, Han J. Critical assessment 19: Stacking fault energies of austenitic steels. Mater. Sci. Technol., 2016, 32(1): 1–8. https://doi.org/10.1080/02670836.2015.1114252.

[35] Wang Y, Zhang Y, Gong W, et al. On the role of austenite stability in yielding behavior of a medium Mn steel with a duplex austenite-martensite microstructure. Acta Mater., 2025, 288: 120840. https://doi.org/10.1016/j.actamat.2025.120840.

[36] Han C S, Gao H, Huang Y, et al. Mechanism-based strain gradient crystal plasticity-I. Theory. J. Mech. Phys. Solids., 2005, 53(5): 1188–1203. https://doi.org/10.1016/j.jmps.2004.08.008.

[37] Kubin L P, Mortensen A. Geometrically necessary dislocations and strain-gradient plasticity: A few critical issues. Scr. Mater., 2003, 48(2): 119–125. https://doi.org/10.1016/S1359-6462(02)00335-4.

[38] Shang X, Zhao J, Li X, et al. The determining role of laminar heterostructures on the mechanical properties of low-density steels. Mater. Sci. Eng. A, 2023, 881: 145340. https://doi.org/10.1016/j.msea.2023.145340.

[39] Wu B B, Wang Z Q, Wang X L, et al. Relationship between high angle grain boundaries and hardness after γ→α transformation. Mater. Sci. Technol., 2019, 35(15): 1803–1814. https://doi.org/10.1080/02670836.2019.1647936.

[40] Hu Y, Niu Y, Zhang Q, et al. Synergistic effect of laves phase evolution and porosity defects in nuclear-grade FeCrAl alloy laser welded joints: Experiments and crystal plasticity modeling. Opt. Laser Technol., 2023, 157: 108694. https://doi.org/10.1016/j.optlastec.2022.108694.

[41] Liu Z, Yang Z, Wang X, et al. Enhanced strength-ductility synergy in a new 2.2 GPa grade ultra-high strength stainless steel with balanced fracture toughness: Elucidating the role of duplex aging treatment. J. Alloys Compd., 2022, 928: 167135. https://doi.org/10.1016/j.jallcom.2022.167135.

[42] Zhu Y, Wu X. Perspective on hetero-deformation induced (HDI) hardening and back stress. Mater. Res. Lett., 2019, 7(10): 393–398. Https://doi.org/10.1080/21663831.2019.1616331.

[43] Kaschner G C, Tomé C N, McCabe R J, et al. Exploring the dislocation/twin interactions in zirconium. Mater. Sci. Eng. A, 2007, 463(1–2): 122–127. https://doi.org/10.1016/j.msea.2006.09.115.

[44] Randle V. Mechanism of twinning-induced grain boundary engineering in low stacking-fault energy materials. Acta Mater., 1999, 47(15–16): 4187–4196. https://doi.org/10.1016/S1359-6454(99)00277-3.

[45] McBee C L, Kruger J. Nature of passive films on iron-chromium alloys. Electrochim. Acta, 1972, 17(8): 1337–1341. https://doi.org/10.1016/0013-4686(72)80079-3.

[46] Oblonsky L J, Devine T M. A surface enhanced raman spectroscopic study of the passive films formed in borate buffer on iron, nickel, chromium and stainless steel. Corros. Sci., 1995, 37(1): 17–41. https://doi.org/10.1016/0010-938X(94)00102-C.

[47] Oh K, Toor I U H, Ahn S, et al. Effects of Cu on the passive film stability of Fe-20Cr-*x*Cu (*x*=0, 2, 4wt.%) alloys in H_2SO_4 solution. Electrochimica Acta, 2013, 88: 170–176. https://doi.org/10.1016/j.electacta.2012.10.058.

[48] Oh K, Ahn S, Eom K, et al. Observation of passive films on Fe-20Cr-*x*Ni (*x*=0, 10, 20wt.%) alloys using TEM and Cs-corrected STEM-EELS. Corros. Sci., 2014, 79: 34–40. https://doi.org/10.1016/j.corsci.2013.10.023.

[49] Asami K, Hashimoto K, Shimodaira S. XPS determination of compositions of alloy surfaces and surface oxides on mechanically polished iron-chromium alloys. Corros. Sci., 1977, 17(9): 713–723. https://doi.org/10.1016/0010-938X(77)90067-1.

[50] Tokuda S, Muto I, Sugawara Y, et al. Pit initiation on sensitized type 304 stainless steel under applied stress: Correlation of stress, Cr-depletion, and inclusion dissolution. Corros. Sci., 2020, 167: 108506. https://doi.org/10.1016/j.corsci.2020.108506.